LASER
&PHOTONICS
REVIEWS

REPRINT

LASER & PHOTONICS REVIEWS

ORIGINAL PAPER

**Abstract** This work presents analytical, numerical and experimental demonstrations of light diffracted through a logarithmic spiral (LS) nanoslit, which forms a type of switchable and focustunable structure. Owing to a strong dependence on the incident photon spin, the proposed LS-nanoslit converges incoming light of opposite handedness (to that of the LS-nanoslit) into a confined subwavelength spot, while it shapes light with similar chirality into a donut-like intensity profile. Benefitting from the varying width of the LS-nanoslit, different incident wavelengths interfere constructively at different positions, i.e., the focal length shifts from 7.5 μm (at $\lambda = 632.8$ nm) to 10 μm (at $\lambda = 488$ nm), which opens up new opportunities for tuning and spatially separating broadband light at the micrometer scale.
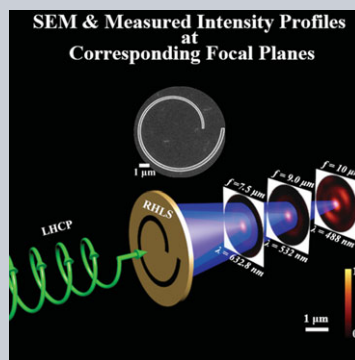
Broadband spin-controlled focusing via logarithmic-spiral nanoslits of varying width

M. Q. Mehmood[1,**], **Hong Liu**[2,**], **Kun Huang**[1], **Shengtao Mei**[1], **Aaron Danner**[1], **Boris Luk'yanchuk**[3], **Shuang Zhang**[4], **Jinghua Teng**[2], **Stefan A. Maier**[5], and **Cheng-Wei Qiu**[1,*]

1. Introduction

The spin property of light with handedness (i.e., circular polarization) is usually examined through use of a quarter wave-plate (QWP) in combination with a linear polarizer (LP). However, owing to emerging applications at small scales, the requirement of having compact circular polarizers and analyzers is highly desirable. To achieve the objective, chiral structures are an appealing choice, as they interact differently with different circular polarizations, resulting in interesting broadband phenomena such as optical activity, polarization conversion and circular dichroism in either planar [1–5] or three-dimensional (3D) metamaterials [6–8]. In order to employ these chiral structures to differentiate between the handedness of incident circular polarization, a gold helix array has been demonstrated as a compact broadband circular polarizer and analyzer in the infrared region, where circularly polarized (CP) light with a handedness opposite to that of the helix's handedness was transmitted while the matching handedness was reflected [9]. Several modifications to this helical structure have also been presented to further enhance the performance of the circular-polarizer, e.g., tapered gold-helix metamaterials [10] and 3D bichiral arrangements [11, 12]. Although

these 3D structures exhibited appealing properties as a circular polarizer or analyzer, their requirements of having a periodic array with subwavelength features with precise alignment created paramount challenges in fabrication.

To overcome the constraints, an innovative approach of layer-by-layer design [13, 14] was found to differentiate between the incident circular polarizations but the performance was not comparable to 3D helix-based structures. An ideal approach would be to employ a single planer structure that can differentiate between the transmitted or reflected circular polarizations of opposite handedness. In this regard, Bachman et al. [15] reported a spiral plasmonic antenna, which could function as a circular polarization transmission filter. However, it suffered meager performance in terms of extinction ratio (ER) and bandwidth. Meanwhile, Yang and Chen et al. [16, 17] demonstrated a unique response from a miniature single-arm Archimedean spiral (AS) grating in the Au film, which could selectively concentrate spinning light of one handedness (opposite to the structural handedness) at the center of the spiral, while light with the other handedness is concentrated into a donut-shaped region with a dark center. Although it was analytically and numerically calculated that a high ER was achievable, the phenomenon was strictly limited in

[1] Department of Electrical and Computer Engineering, National University of Singapore, 4 Engineering Drive 3, Singapore 117583
[2] Institute of Materials Research and Engineering, Agency for Science, Technology and Research (A*STAR), 3 Research Link, Singapore 117602
[3] Data Storage Institute, Agency for Science, Technology and Research (A*STAR), DSI Building, 5 Engineering Drive 1, Singapore 117608
[4] School of Physics & Astronomy, University of Birmingham, Birmingham, B15 2TT, UK
[5] The Blackett Laboratory, Department of Physics, Imperial College London, London, SW7 2 AZ, UK
[**]These Authors contributed equally to this work.
[*]Corresponding author: e-mail: eleqc@nus.edu.sg

use to near-field regions due to the involvement of surface plasmons (SP) that decay exponentially away from the surface of the structure. Experimental observation of this phenomenon was attempted through near-field scanning optical microscopy (NSOM), but significant challenges were encountered in the detection of a solid spot due to the sensitivity of the NSOM probe [17]. In a subsequent study, this limitation was overcome to some degree by employing two-photon fluorescence microscopy [18] but the results were still not perfect. Several other planar structures have also been studied that carry potential for use as circular polarization analyzers or polarizers [19–22], but the availability of an easily engineered and characterizable, compact broadband circular polarization analyzer (in the visible spectrum) with descent performance remains a challenge.

In this work, we propose a single-turn LS-nanoslit as a compact polarization analyzer in the meso-field. In contrast to the aforementioned AS, our structure is capable of achieving decent performance using constructive interference of light with well-defined handedness, diffracted through the LS-nanoslit, rather than from an excited SP wave. The intensity profile at the focal plane is rigorously dictated by the handedness of the CP excitation and that of the LS-nanoslit. ER of ≈ 100 can be obtained, at the focal plane, in a circular region of interest of 100 nm diameter at $\lambda = 532$ nm. The proposed structure can provide efficient focusing and could be a promising candidate for full Stokes parameter polarimetric imaging applications, where detecting complete Stokes parameters is a challenging task due to the lack of inexpensive and compact microdevices that can differentiate between left- and right-hand circularly polarized (LHCP and RHCP) illuminations.

2. Materials and methods

Before presenting experimental details, we present an analytical description of the problem. A right-hand logarithmic spiral (RHLS) structure along with a coordinate setup to analytically calculate the diffracted light is depicted in Fig. 1a. The mathematical description of the RHLS structure in cylindrical coordinates is expressed as $r = a.e^{b.\varphi}$, where 'r' and 'φ' indicate the radial and angular coordinates at the aperture plane ($z = 0$), respectively, while 'a' and 'b' are arbitrary positive constants [23]. The radial factor a determines the starting radius and the azimuthal factor b controls the direction and speed of angular growth, whereas overall compactness of the structure is governed collectively by them. At the observation plane, i.e., $z = f$ (focal plane); denotes the radial distance and 'θ' represents the azimuthal angle, while 'z' is the distance between two planes and 'R' is the distance from the source (LS-nanoslit in this case) to the field calculation point at the observation plane as illustrated in Fig. 1a. It is well known that a CP beam can be described in cartesian and cylindrical coordinate systems as follows:

$$E_{CP} = \frac{1}{\sqrt{2}}(e_x \pm i.e_y) = \frac{1}{\sqrt{2}}e^{\pm i.\varphi}(e_r \pm i.e_\varphi). \quad (1)$$

This elucidates that the circular polarization is fundamentally a combination of radial and azimuthal beams with a spiral wavefront. The radial and azimuthal components are transverse electric (TE) and transverse magnetic (TM) polarized with respect to the LS-nanoslit. The corresponding electric-field components (in terms of the cylindrical coordinates) can be expressed as; $E_r = e^{\pm i.\varphi}$ and $E_\varphi = \pm i.e^{\pm i.\varphi}$. The interaction of this added spiral wavefront with the LS-nanoslit plays a pivotal role in defining the intensity distribution at the focal plane, which ultimately ensues in identifying the incident photon spin.

To corroborate this reasoning, foremost we numerically study the response ($|E|^2$) of a single ring with subwavelength slit-width (width = 0.35 μm and inner radius = 3.5 μm) under LHCP and RHCP illuminations. As expected, the symmetric nature of the ring-slit is incapable of differentiating between the opposite handedness of incident CP light as depicted in Fig. S1. It is important to mention here that we are looking at the overall intensity ($|E|^2$) instead of left- ($|E_L|^2$) and right- ($|E_R|^2$) handed intensity distributions, because the occurrence of birefringence [24], in the case of rings with a subwavelength slit width, is beyond our interest. Moreover, it is found that the LS-nanoslit is functioning as a parallel-plate metal waveguide, where the azimuthal component (with spiral phase front) is propagating through the LS-nanoslit while the radial component (with spiral component) is decaying. To investigate this further, we used the following vectorial Rayleigh–Sommerfeld (VRS) [25] equations to analytically deduce the transmitted field of the structure.

$$E_r(\rho, \theta, z) = \frac{-1}{2\pi} \int_0^{2\pi} \int_{r_1}^{r_2} \left[E_r(r, \varphi, 0)\cos(\varphi - \theta) \right. $$
$$\left. - E_\varphi(r, \varphi, 0)\sin(\varphi - \theta) \right] \left(ikn - \frac{1}{R} \right)$$
$$\times \left(\frac{z}{R^2} \exp(iknR) \right) rdrd\varphi \quad (2)$$

$$E_\varphi(\rho, \theta, z) = \frac{-1}{2\pi} \int_0^{2\pi} \int_{r_1}^{r_2} \left[E_\varphi(r, \varphi, 0)\cos(\varphi - \theta) \right. $$
$$\left. + E_r(r, \varphi, 0)\sin(\varphi - \theta) \right] \left(ikn - \frac{1}{R} \right)$$
$$\times \left(\frac{z}{R^2} \exp(iknR) \right) rdrd\varphi \quad (3)$$

$$E_z(\rho, \theta, z) = \frac{1}{2\pi} \int_0^{2\pi} \int_{r_1}^{r_2} \left[E_r(r, \varphi, 0)\{r - \rho\cos(\varphi - \theta)\} \right. $$
$$\left. + E_\varphi(r, \varphi, 0)\rho\sin(\varphi - \theta) \right] \left(ikn - \frac{1}{R} \right)$$
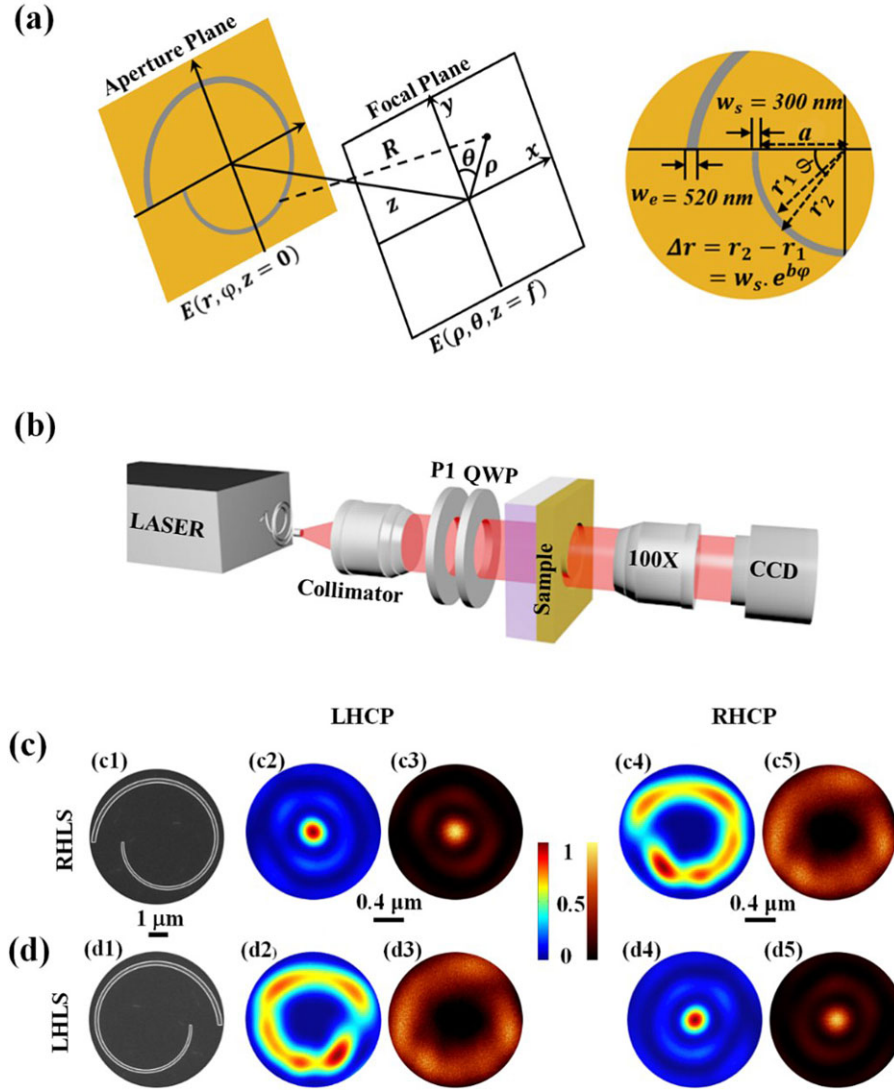$$\times \left(\frac{1}{R^2} \exp(iknR) \right) rdrd\varphi \quad (4)$$

Figure 1 Experimental setup, pictorial description for analytical formulation, SEM images and *xy*-plane intensity profiles at the focal plane ($z = 7.5$ μm). The color scale in each intensity image is normalized to its respective maximum intensity. (a) Schematic illustration of a RHLS-nanoslit and polar coordinate system setup for analytically calculating the field distributions of light diffracted from the LS-nanoslit. The right side is the inset of aperture plane showing the details of geometric parameters. (b) Experimental setup for measuring the transmitted intensity distribution. It includes QWP in combination with LP (P1) to obtain the CP illumination, a collimator, a laser and an objective lens. (c) Intensity mappings across the center of the RHLS-nanoslit (c1) under LHCP (c2 and c3) and RHCP (c4 and c5) illuminations. (d) Intensity profiles across the center of the LHLS-nanoslit (d1) under LHCP (d2 and d3) and R'HCP (d4 and d5) illuminations.

In the above equation, $R^2 = z^2 + \rho^2 + r^2 - 2\rho r \cos(\varphi - \theta)$, '$k = 2\pi/\lambda$' represents the wave-vector and 'n' is the refractive index of the background medium ($n = 1$ for the current case), while $r_1 = a.e^{b.\varphi}$ and $r_2 = (a + w_s).e^{b.\varphi}$ The values of a and b are taken as 3.5 μm and 0.0875, respectively, while starting (w_s) and ending (w_e) widths of LS-nanoslit are 300 nm and 520 nm, respectively, as shown in Fig. 1a.

Now, inserting $E_\varphi = \pm i.e^{\pm i.\varphi}$ and ignoring the radial field component (due to the sole contribution from the azimuthal component) lead to the following simplified VRS expressions

$$E_r(\rho, \theta, z) = \frac{\pm i}{2\sqrt{2}\pi} \int_0^{2\pi} \int_{r_1}^{r_2} i.e^{\pm i.\varphi} \sin(\varphi - \theta) \left(ikn - \frac{1}{R}\right)$$

$$\times \left(\frac{z}{R^2} \exp(iknR)\right) r dr d\varphi \tag{5}$$

$$E_\varphi(\rho, \theta, z) = \frac{\pm i}{2\sqrt{2}\pi} \int_0^{2\pi} \int_{r_1}^{r_2} i.e^{\pm i.\varphi} \cos(\varphi - \theta) \left(ikn - \frac{1}{R}\right)$$

$$\times \left(\frac{z}{R^2} \exp(iknR)\right) r dr d\varphi \tag{6}$$

$$E_z(\rho, \theta, z) = \frac{\mp i}{2\sqrt{2}\pi} \int_0^{2\pi} \int_{r_1}^{r_2} i.\rho.e^{\pm i.\varphi} \sin(\varphi - \theta) \left(ikn - \frac{1}{R}\right)$$

$$\times \left(\frac{1}{R^2} \exp(iknR)\right) r dr d\varphi. \tag{7}$$

Guided by the analytical formulation, we specifically fabricated left- and right-handed LS (LHLS and RHLS) structures, where a 350-nm thick Au film was deposited onto a fused quartz substrate (UV grade, 15 mm (W) ×

15 mm (L) $\times$ 0.4 mm (H)) by electron-beam vapor deposition (Denton Vacuum, Explorer) at room temperature under a vacuum pressure of 5×10^{-7} Torr. Owing to the wave-guiding properties of the LS-nanoslit, the metal film was purposely made thick enough to be considered as a waveguide [26, 27]. Indeed, we observed that metal films of a smaller thickness (< 200 nm) exhibit a significantly degraded device performance. After the deposition process, positive resist (ZEP520A) was coated to achieve the desired thickness and backed on a hotplate for two minutes at 180 ºC. For electron-beam lithography (ELS-7000, Elionix), both LHLS and RHLS structures were patterned onto the resist by development in o-Xylene for a period of 30 s. Later, the developed pattern of the LS-nanoslit was etched into the Au film through dry etching process (Nanoquest, Intlvac) under a suitable exposure time. Eventually, the LS-nanoslits, milled into the Au film with a minimum feature size of ≈ 300 nm, were ready. Owing to the substantial thickness of the Au film, the incident CP light can be transmitted through the LS-nanoslit, while it is entirely blocked elsewhere by the rest of the Au film. Figures 1c1 and d1 show scanning electron microscope (SEM) images of RHLS and LHLS structures respectively, where the overall size of an individual spiral structure is about 11 μm.

3. Results and Discussions

Figures 1 (cf. c2, d2, c4 and d4) present the field distribution, obtained from Eqs. (5)–(7) at the focal plane ($z = 7.5$ μm) under both cases of azimuthal components ($i.e^{i.\varphi}$ and $-i.e^{-i.\varphi}$) corresponding to LHCP and RHCP illuminations at $\lambda = 632.8$ nm. The results illustrate the anticipated phenomenon of spin-controlled intensity mapping at the observation plane. Afterwards, we numerically (through FDTD Lumerical) simulated our structure with azimuthal ($E_\varphi = \pm i.e^{\pm i.\varphi}$) and radial ($E_r = e^{\pm i.\varphi}$) source profiles. The results, given in Figs. S4 and S5, explicate the aforementioned reasoning that focal plane intensity profiles are mainly dictated by the azimuthal component of the incident CP light, whereas the role of radial component is negligible.

Following the analytical analysis, we characterized our samples (both RHLS and LHLS) under oppositely handed incident illuminations (i.e. LHCP and RHCP). Schematic diagram of the measurement setup is depicted in Fig. 1b, where a collimated optical beam was converted to CP beam through a QWP in combination with a LP before impinging on the structure. For single wavelength characterization; we used HeNe Laser ($\lambda = 632.8$ nm), while broadband measurements included Nd-YAG ($\lambda = 532$ nm) and DPSS ($\lambda = 488$ nm) lasers as well. The transmitted intensity was collected by photon scanning tunneling microscope (PSTM) after passing through an objective lens (of $100\times$). Our PSTM system is WITEC alpha 300S, which can perform AFM, confocal, Raman and near-field scanning microscopy (NSOM) characterization. For the characteri-

zation of the transverse intensity profile in this work, we only utilized the confocal imaging of this PSTM system. Figure 1 (cf. c3, d3, c5 and d5) illustrates the measurement results at $\lambda = 632.8$ nm, which give excellent agreement to analytically obtained outcomes; hence validating the anticipated spin-controlled phenomenon. Figure S6 illustrates that the measured full wave half-maximum (FWHM) of $\approx 0.65\lambda$ and $\approx 0.70\lambda$ at corresponding focal planes are achieved under illumination wavelengths of 532 nm and 632.8 nm, respectively.

It is worth noting that the spin-controlled focusing (dictated by the LS-nanoslit) does not deteriorate much by fixing the observation plane under different incident wavelengths (within the operational bandwidth). In this regard, we numerically calculated the ERs at a fixed plane of $z = 9.5$ μm under different incident wavelengths, ranging from 440 nm to 800 nm with a step size of 20 nm. The insets of Figs. 2a and b demonstrate the method to calculate the ER, where corresponding field intensities within the circular areas (100 nm diameter) are integrated. The position where the maximum intensity exists for the case of focus spot (RHLS under RHCP illumination), was taken as the center of the circular integration area for both cases (RHLS LS-nanoslit under both LHCP and RHCP illuminations). The normalized ERs (to the maximum value at $\lambda = 620$ nm) are plotted in Fig. 2a and the bandwidth is defined as the span of wavelengths over which the ER is larger than the half of the maximum value. The calculated results predict that the working bandwidth of our device ranges from $\lambda = 520$ nm to $\lambda = 720$ nm with a peak value at $\lambda = 620$ nm. Within this range, the calculated ERs are above half of the maximum value. Owning to the availability of two laser sources ($\lambda = 632.8$ nm and 532 nm) within this range, we calculated the ERs from the measured data for various diameters (from 100 nm to 2000 nm) and plotted them in Fig. 2b along with simulation data. The experimentally obtained results demonstrate that ERs of ≈ 80 and ≈ 100 are achievable for a smaller region of interest (≈ 100 nm diameter) at working wavelengths of 632.8 nm and 532 nm, respectively. The fine agreement between the simulation and measured data, at these two wavelengths, reveals that the device will function reasonably within the entire predicted bandwidth.

Apart from calculating the ERs, we have numerically calculated the focusing efficiency (FE) by varying the incident wavelength from 440 nm to 800 nm as shown in Fig. S7. The FE is defined as a ratio between the integrated intensity of the focal spot (i.e., circular region of interest of 1000 nm diameter at $\lambda = 9.5$ μm) and the transmitted intensity through the LS-nanoslit. Across the bandwidth ($\lambda = 520$–720 nm), FE varies its amplitude from $\approx 80\%$ to the maximal. It is observed, from the numerical calculations, that the FE at $\lambda = 532$ nm is $\approx 90\%$ of that at $\lambda = 632.8$ nm, which is dually confirmed through the measured results where the FE at $= 532$ nm is equivalent to $\approx 91\%$ of that at $\lambda = 632.8$ nm. Hence, a good agreement between the simulation and experimental results is found in terms of FE as well. In addition, we also compared the simulation and measured intensity profiles at $z = 9.5$ μm under
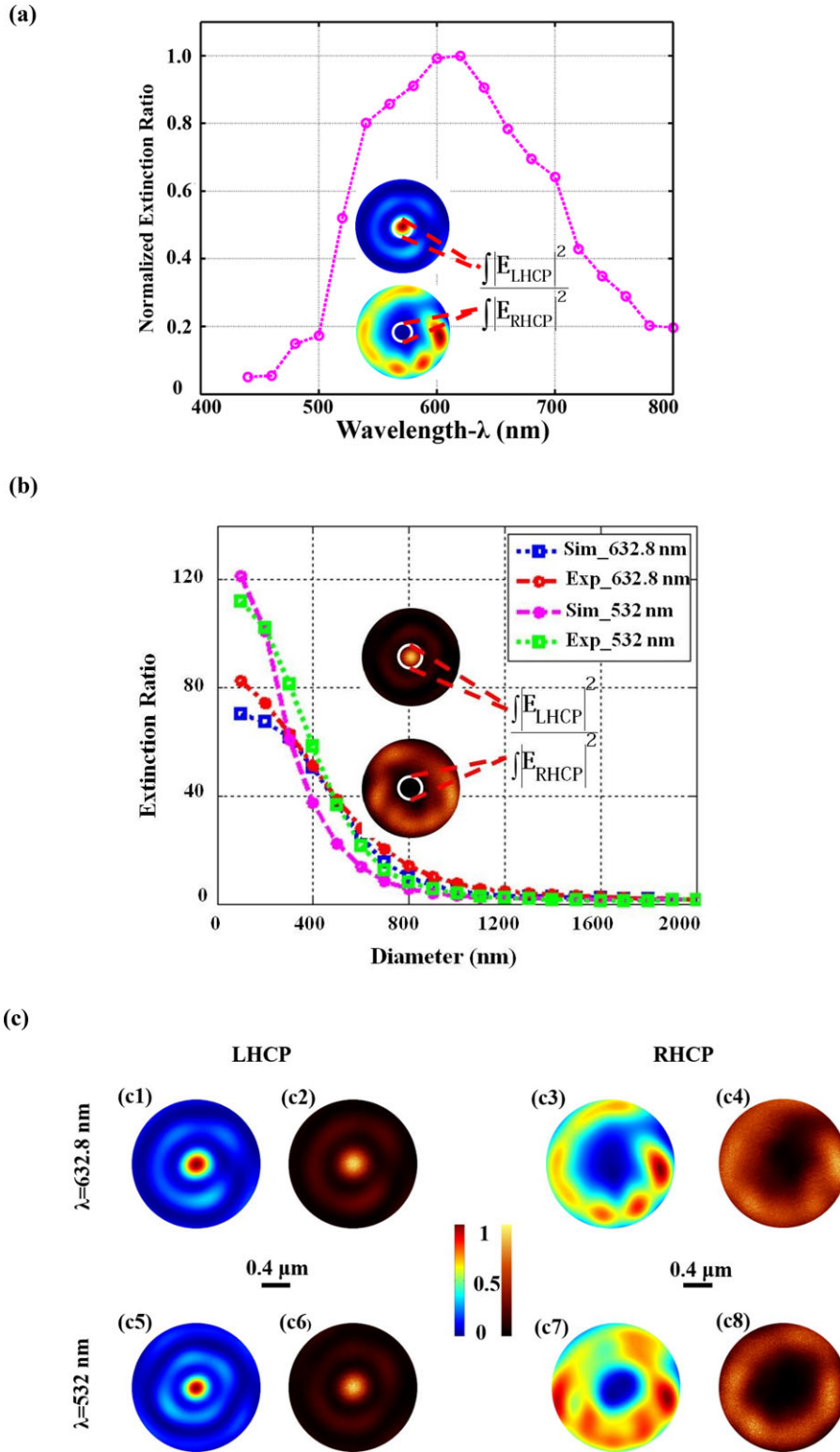
(a)

(b)

(c)

Figure 2 ER and transverse intensity profiles, at the fixed observation plane of $z = 9.5$ μm, of RHLS-nanoslit: (a) Simulation results of normalized ER for the incident wavelengths, ranging from 400 nm to 800 nm. Inset illustrates the pictorial depiction of the methodology, adopted to calculate the ER. (b) Comparison between the measured and calculated ERs with respect to the circular region of interest at incident wavelengths of 632.8 nm and 532 nm. Inset illustrates the pictorial depiction of the methodology, adopted to calculate the ER. (c) Simulation and experimental intensity profiles at = 9.5 μm under LHCP illumination of λ = 632.8 nm and 532 nm.

the incident wavelength of $\lambda = 532$ nm and 632.8 nm to examine the preservation of spin-controlled phenomenon. The results plotted in Fig. 2c illustrate that the desired phenomenon exists at both cases validated by a good agreement between the simulation and experimental results.

Based on the analysis over the broadband range, it is quite convincing that working bandwidth of the device is from 520 nm to 720 nm.

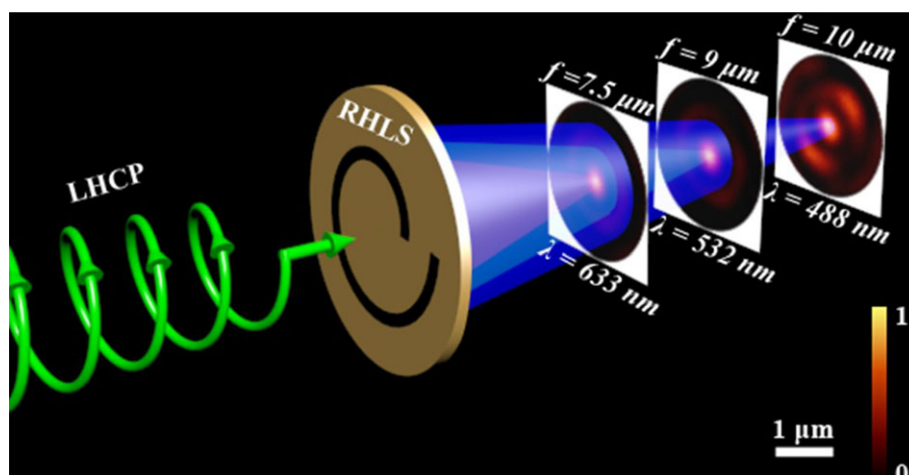Furthermore, we determined that the logarithmic nature of the proposed spiral nanoslit facilitates a response

Figure 3 Measurement results exhibiting the broadband response of the RHLS under LHCP illumination. Focal planes shift from 7.5 μm to 10 μm by varying the incident wavelength from 632.8 nm to 488 nm. The color scale in each intensity image is normalized to its respective maximum intensity.

to a wide range of incident wavelengths (in the visible spectrum), without losing its functioning aptitude of circular polarization differentiation. Broadband analyses of the RHLS structure (under LHCP illumination) have revealed an interesting phenomenon of extraordinary chromatic aberration (ECA), i.e., different incident wavelengths are focused at different longitudinal positions along the axis of the LS-nanoslit. Chromatic aberration (CA) is generally considered as a drawback for a conventional refractive lens, where the focal length is large (in millimeters or centimeters) [28]. However, because of the micrometer-scale focal length of our case, this longitudinal CA is extraordinary and can be exploited to spatially separate different incident wavelengths, where the focal length can be tuned from 7.5 μm to 10 μm by altering the incident wavelength from 632.8 nm to 488 nm as depicted in Fig. 3. By comparing this focal-length shift to the case of a conventional dielectric lens, where it is difficult to have such a dynamic control due to small chromatic dispersion, unveils that the wavelength-tunable shift in our case is much higher [28]. Such a strong effect suggests a technique of controlling the focal length of a LS-nanoslit by changing the illumination wavelength over the visible spectrum and could open up interesting opportunities for novel applications. This value-added merit of the proposed device may open up opportunities for novel applications, e.g., a readout device for color separation scheme, such as color splitter. In practice, the detector can be installed in a xy-stage or optical track to move along the optical axis so that it can measure the focal spots. It is a simple experiment to be set up in the lab or on site.

Apart from the abovementioned observations, we also fabricated RHLS structures with different starting radii ($a=$ 2.5 and 3 μm), but same starting ($w_s = 300$ nm) and ending ($w_e = 520$ nm) LS-nanoslit widths, and compared them with the initial design ($a = 3.5$ μm) to investigate the optical transmission response to the numerical aperture of the LS-nanoslit. All three RHLSs are fabricated on the same

glass substrate to facilitate characterization, and tested under LHCP illumination at a wavelength of 632.8 nm. Figure 4 depicts the field distribution along the xy-plane (cf. Figs. 4a2, b2, c2, a3, b3 and c3) at corresponding focal lengths and along the xz-plane (cf. Figs. 4a4, b4, c4 a5, b5 and c5) of the three different samples on the transmission side. The intensity maps obtained from FDTD simulations (cf. Figs. 4a2, b2, c2, a4, b4 and c4) and experiments (cf. Figs. 4a3, b3, c3, a5, b5 and c5) for each structure are plotted adjacently for comparison. It is found that the diffracted light is strongly focused at the focal planes of 3.5 μm, 5.5 μm and 7.5 μm for the starting radii of 2.5 μm, 3 μm and 3.5 μm, respectively.

It is worth pointing out that the working principle and performance of our LS-nanoslit is different from the spiral plasmonic antenna [15] and AS [17], which behaved as a circular polarization transmission filter and as a circular polarization analyzer, respectively. They were designed for a single operational wavelength, where circular polarization transmission filter of [15] had lower ER (compared to our LS-nanoslit) and circular polarization analyzer of [17] was restricted to the near field. Mathematically our design is based on the algorithm of LS denoted by ($r = a.e^{b.\varphi}$), in which the rotation angle φ is an exponential function of r. In comparison, an AS denoted by $r = a + b\varphi$ in [17], in which the rotation angle φ is a linear function of r. Due to this fundamental difference between these two structures (LS and AS), they interacted differently from incident CP light. The exponential function of LS enables higher degree of freedom (DoF) to acquire broadband behavior and longer focal length and depth while the linear function of AS limits its DoF acting as a single-wavelength device. The AS was designed for a certain plasmonic wavelength (λ_{SPP}) and the phenomenon of incident spin detection was strictly limited to the near-field regions due to the involvement of SP that decay exponentially away from the surface of the structure. Compare to AS, the LS is based on diffractive optics, which can focus light in the meso-field.
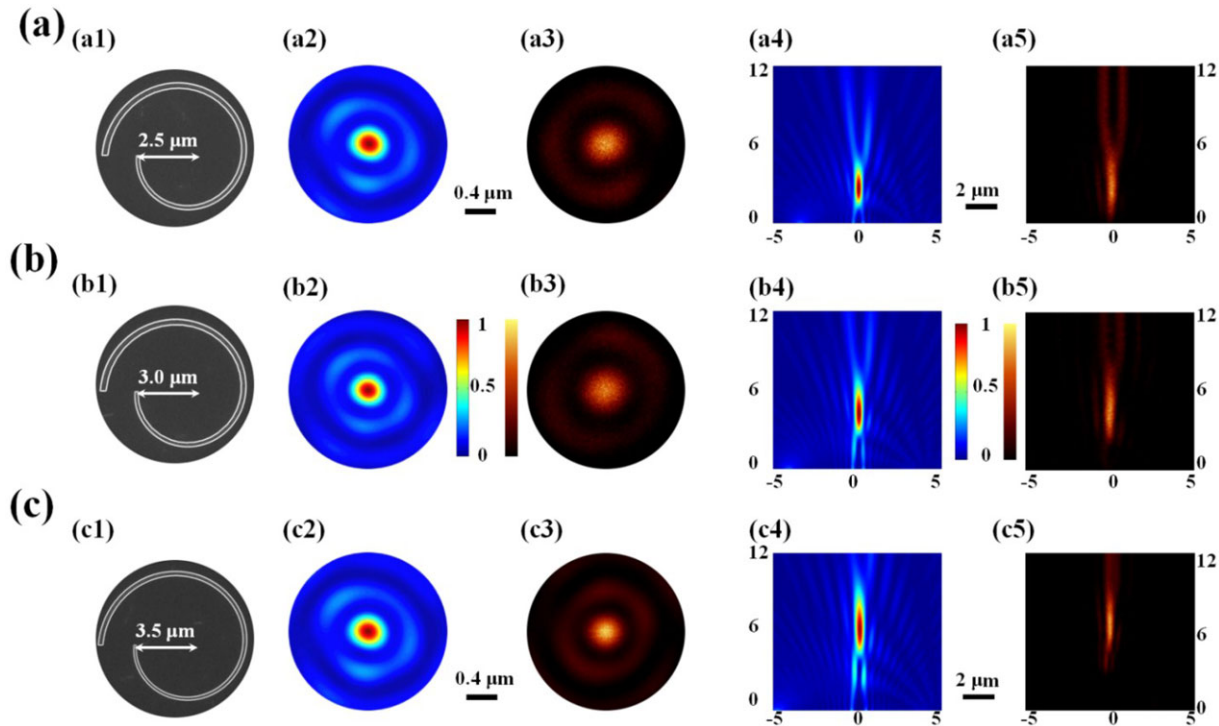
Figure 4 Comparison between numerical and experimental intensity profiles of three differently sized RHLS structures illuminated by LHCP ($\lambda = 632.8$ nm). The color scale in each intensity image is normalized to its respective maximum intensity. (a) Intensity mappings of the RHLS structure with a starting radius of 2.5 μm ($f = 3.5$ μm). (b) Intensity mappings of the RHLS structure with a starting radius of 3 μm ($f = 5.5$ μm). (c) Intensity mappings of the RHLS structure with a starting radius of 3.5 μm ($f = 7.5$ μm). (a2, a3, b2, b3, c2 and c3) Simulated (a2, b2 and c2) and measured (a3, b3 and c3) xy-plane intensity mappings at the corresponding focal planes. (a4, a5, b4, b5, c4 and c5) Simulated (a4, b4 and c4) and measured (a5, b5 and c5) xz-plane field profile.

4. Conclusions

To conclude, we have demonstrated a planar LS-nanoslit as a compact broadband circular polarization analyzer in the meso-field by focusing light of different handedness into a subwavelength confined spot or a ring-shaped intensity profile. Characterization of the fabricated LS-nanoslit, via optical confocal imaging, and corresponding simulations reveal that a circular polarization ER of ≈ 100 can be achieved with a structure size of 11 μm, whereas the device will work across the visible spectrum. We observed that a wavelength-controllable focal plane can be achieved, as the LS-nanoslit exhibits ECA in comparison with conventional lenses, manifesting its ability to spatially separate different incident wavelengths at the micrometer-scale. We have also presented simulation and measurement results for samples of different sizes to illustrate that enlargement of the LS-nanoslit increases its focal length.

Supporting Information

Additional supporting information may be found in the online version of this article at the publisher's website.

Author contributions. M.Q.M. and C.-W.Q. conceived the idea. M.Q.M. optimized the design, helped in the fabrication, and performed the characterization. M.Q.M., K.H., M.S., and C.-W.Q. carried out the computational analysis. H.L. fabricated the sample and helped in characterizations. M.S.Z. contributed to the dry etching process. A.D., B.L., S.Z., S.M., J.H.T., and C.-W.Q. were involved in the analysis of the measured results. M.Q.M., H. L., K. H., M.S., A.D., J.H.T., S.A.M. and C.-W.Q. lead the technical discussions and prepared the manuscript. C.-W.Q. supervised the project.

References

[1] A. V. Rogacheva, V. A. Fedotov, A. S. Schwanecke, and N. I. Zheludev, Phys. Rev. Lett. **97,** 177401 (2006).

[2] S. Takahashi, A. Potts, D. Bagnall, N. I. Zheludev, and A. V. Zayats, Opt. Commun. **255,** 91–96 (2005).

[3] M. Kuwata-Gonokami, N. Saito, Y. Ino, M. Kauranen, K. Jefimovs, T. Vallius, et al., Phys. Rev. Lett. **95,** 227401 (2005).

[4] A. Papakostas, A. Potts, D. M. Bagnall, S. L. Prosvirnin, H. J. Coles, and N. I. Zheludev, Phys. Rev. Lett. **90,** 107404 (2003).

[5] S. L. Prosvirnin and N. I. Zheludev, Phys. Rev. E **71,** 037603 (2005).

[6] A. Guerrero-Martinez, B. Auguie, J. L. Alonso-Gomez, Z. Dzolic, S. Gomez-Grana, M. Zinic, et al., Angew. Chem. Int. Edit. **50,** 5499–5503 (2011).

[7] B. Frank, X. H. Yin, M. Schaferling, J. Zhao, S. M. Hein, P. V. Braun, et al., ACS Nano **7,** 6321–6329 (2013).

[8] M. Esposito, V. Tasco, M. Cuscunà, F. Todisco, A. Benedetti, I. Tarantini, et al., ACS Photon. **2,** 105–114 (2015).

[9] J. K. Gansel, M. Thiel, M. S. Rill, M. Decker, K. Bade, V. Saile, et al., Science **325,** 1513–1515 (2009).

[10] J. K. Gansel, M. Latzel, A. Frölich, J. Kaschke, M. Thiel, and M. Wegener, Appl. Phys. Lett. **100,** 101109 (2012).

[11] M. Thiel, M. S. Rill, G. vonFreymann, and M. Wegener, Adv. Mater. **21,** 4680–4682 (2009).

[12] A. Radke, T. Gissibl, T. Klotzbucher, P. V. Braun, and H. Giessen, Adv. Mater. **23,** 3018–3021 (2011).

[13] M. Thiel, G. vonFreymann, and M. Wegener, Opt. Lett. **32,** 2547–2549 (2007).

[14] Y. Zhao, M. A. Belkin, Aand . Alu, Nature Commun. **3,** 870 (2012).

[15] K. A. Bachman, J. J. Peltzer, P. D. Flammer, T. E. Furtak, R. T. Collins, and R. E. Hollingsworth, Opt. Exp. **20,** 1308–1319 (2012).

[16] S. Yang, W. Chen, R. L. Nelson, Q. Zhan, Opt. Lett. **34,** 3047–3049 (2009).

[17] W. Chen, D. C. Abeysinghe, R. L. Nelson, and Q. Zhan, Nano. Lett. **10,** 2075–2079 (2010).

[18] Z. Wu, W. Chen, D. C. Abeysinghe, R. L. Nelson, and Q. Zhan, Opt. Lett. **36,** 1244–1244 (2011).

[19] E. Plum, V. A. Fedotov, and N. I. Zheludev, Appl. Phys. Lett. **94,** 131901 (2009).

[20] A. V. Krasavin, A. S. Schwanecke, N. I. Zheludev, M. Reichelt, T. Stroucken, S. W. Koch, et al., Appl. Phys. Lett. **86,** 201105 (2005).

[21] Y. Q. Ye, X. Li, F. Zhuang, and S. W. Chang, Appl. Phys. Lett. **99,** 031111 (2011).

[22] H. X. Xu, G. M. Wang, M. Q. Qi, T. Cai, and T. J. Cui, Opt. Exp. **21,** 24912–24921 (2013).

[23] H. Liu, M. Q. Mehmood, K. Huang, L. Ke, H. P. Ye, P. Genevet, et al., Adv. Opt. Mater. **2,** 1193–1198 (2014).

[24] P. F. Chimento, Alkemade PFA, G. W. 't Hooft, and E. R. Eliel, Opt. Lett. **37,** 4946–4948 (2012).

[25] H. P. Ye, C. W. Qiu, K. Huang, J. H. Teng, B. Luk'yanchuk, and S. P. Yeo, Laser Phys. Lett. **10,** 065004 (2013).

[26] S. Ishii, A. V. Kildishev, V. M. Shalaev, K. P. Chen, and V. P. Drachev, Opt. Lett. **36,** 1244–1244 (2011).

[27] S. Ishii, V. M. Shalaev, and A. V. Kildishev, Nano Lett. **13,** 159–163 (2013).

[28] P. Khare and A. Swarup. Engineering Physics: Fundamentals and Modern Applications (Infinity Science Press, 2007).